

# A study on the energy transfer of a square prism under fluid-elastic galloping

H.G.K.G. Jayatunga, B.T. Tan, J. S. Leontini

---

## Abstract

In this paper, power transfer of an elastically mounted body under the influence of fluid-elastic galloping is analysed.

The quasi-steady state model equations are first analysed to find suitable governing parameters. It is shown that, as well as  $Re$ , the system is a function of three dimensionless groups: a combined mass-stiffness parameter  $\Pi_1$ ; a combined mass-damping parameter,  $\Pi_2$ ; and mass ratio  $m^*$ .

Data obtained by numerically integrating the quasi-steady state equations show that for high values of  $\Pi_1$ , the power extracted from the flow is a function of  $\Pi_2$  only. For low values of  $\Pi_1$ , the power extracted is still a strong function of  $\Pi_2$ , but is also a weak function of  $\Pi_1$ . For all the cases tested, the power extracted was independent of the value of  $m^*$ .

These results are then compared to results of direct numerical simulations. It is found that  $\Pi_1$  has a much stronger impact on the power extracted than predicted by the quasi-steady state model. The error is shown to be an inverse function of  $\Pi_1$ . The failure of the quasi-steady state model at low  $\Pi_1$  is hypothesised to be due to the stronger influence of vortex shedding, which is not accounted for in the quasi-steady model. Spectral analysis of the DNS cases at low  $\Pi_1$  shows a significant response at the vortex shedding frequency. The strength of the vortex shedding response is also shown to be an inverse function of  $\Pi_1$ .

Even though the quasi-steady model does not accurately predict the power extracted, it does predict the parameter values at which maximum power transfer occurs reasonably well, and both the quasi-steady model and the direct numerical simulations show this value is basically independent of  $\Pi_1$ .

*Keywords:* Fluid-structure interaction, transverse galloping.

---

## 1. Introduction

Transverse fluid-elastic galloping is one phenomenon in the broader class of phenomena of fluid structure interactions. This area has been of interest due to the vibrations created by galloping on transmission lines (Parkinson and Smith, 1964) and other civil structures, leading to failure either through high peak loads or the cumulative effect of fatigue. Therefore understanding this phenomenon in order to suppresses these vibrations has been an important research task. However, the search for alternate energy sources with minimal environmental impact has become an important area of research in the modern word. Therefore researchers are moving towards investigating the possibility of extracting useful energy from these vibrations by encouraging rather than suppressing them (Barrero-Gil et al., 2010). Hence, in this paper the power transfer from the fluid to the body, and the governing parameters influencing it, are investigated, with a focus on identifying conditions that lead to optimum power transfer.

According to Païdoussis et al. (2010), Glauert (1919) provided a criterion for the onset of galloping by considering the auto-rotation of an aerofoil. Den Hartog (1956) provided a theoretical explanation for galloping for iced electric transmission lines. A weakly non-linear theoretical aeroelastic model to predict the response of galloping was developed by Parkinson and Smith (1964) based on a quasi-steady state (QSS) hypothesis. This hypothesis simply claims that only the time-mean lift on the body (averaged over a time much longer than any vortex shedding period) contributes to the dynamics. Lift forces measured experimentally on a static square prism at different angles of attack were used as an input for the theoretical model. This relatively simple model achieved a remarkably good agreement with galloping experiments conducted in a wind tunnel, where the vortex shedding frequency was much higher than the eventual body oscillation frequency, due to the body being relatively heavy.

However, the QSS model equation, when solved analytically assuming a sinusoidal solution, is not as accurate for cases where the body is relatively light, such as occurs in fluid-dynamic applications. Joly et al. (2012) observed that finite element simulations show a sudden change in amplitude below a critical value of the mass ratio  $m^*$ . The QSS model derived in Parkinson and Smith (1964) was altered to account for the vortex shedding and solved numerically to predict the reduced displacement amplitude at low mass ratios to the point where galloping is no longer present. While a reasonable

agreement could be found, the model still required a parameter to be tuned to find the best match.

Most of the literature on galloping using the QSS model has been focused on predicting the displacement amplitude (Parkinson and Smith, 1964; Joly et al., 2012; Luo et al., 2003). However, it is quite important to analyse the behaviour of the velocity when studying the power transfer from the fluid to the body. This is because instantaneous power from the fluid flow to the system is the product of the fluid dynamic force and the velocity of the system while instantaneous power out of the system is the product of the damping and the velocity of the system. The fluid dynamic force is also modelled to be only dependent on the velocity of the system. This study also focuses on how well the QSS model performs at high damping at low Reynolds numbers.

Here, the modified QSS model is integrated numerically and the power transfer from the fluid to the body is investigated, similar to the study of Barrero-Gil et al. (2010). Two different values of  $Re$  are tested:  $Re = 200$ , a case that should remain laminar and closer to two-dimensional behaviour;  $Re = 22300$ , a case where the flow is expected to be turbulent and three-dimensional. The QSS model requires the lift or transverse force coefficient,  $C_y$  as a function of angle of attack  $\theta$  for a fixed body. These data were provided from direct numerical simulations for the  $Re = 200$  case, while the data provided by Parkinson and Smith (1964) are used for the  $Re = 22300$  case.

The structure of the paper is as follows. Section 2 presents the governing equations and the QSS model and introduces the method for the calculation of the power transferred from the fluid to the structure. In section 3 a set of non-dimensional governing parameters are derived from the QSS model by considering the relevant time scales in the system. These parameters are a combined mass-stiffness  $\Pi_1$  and a combined mass-damping  $\Pi_2$ . The response characteristics predicted by the integration of the QSS model for both the high and low  $Re$  cases are then presented in terms of these parameters, and it is shown that the power transfer is primarily a function of  $\Pi_2$ . However, when  $\Pi_1$  is low, the power transfer is also predicted to be a weak function of  $\Pi_1$ . For the low  $Re$  case, the results of the QSS model are then compared to those of direct numerical simulations (DNS) of the fluid-structure interaction problem. It is shown that there is a large discrepancy between the predictions of power transfer from the QSS model and the DNS simulations when  $\Pi_1$  is low. This is hypothesised to be due to the influence of vortex shedding which is not accounted for in the QSS model. Spectral data showing an increasing

influence of the vortex shedding frequency in the system response is presented to support this hypothesis. While the QSS model does not accurately predict the value of power transfer, it does predict the parameter values at which maximum power transfer occurs reasonably well. Considering the simplicity of the model, and the minimal computational resources it requires compared to the DNS model, the QSS model can therefore be used as a valuable design tool for power extraction devices. Finally, section 4 presents the conclusions that can be drawn from this work.

## Nomenclature

|                         |  |
|-------------------------|--|
| $a_1, a_3, a_5, a_7$    | Coefficients of the polynomial to determine $C_y$                    |
| $A$                     | Displacement amplitude   |
| $c$                     | Damping constant   |
| $D$                     | Characteristic length (side length) of the cross section of the body |
| $f = \sqrt{k/m}/2\pi$   | Natural frequency of the system                                      |
| $f_g$                   | Frequency of galloping   |
| $f_s$                   | Frequency of vortex shedding   |
| $F_y$                   | Instantaneous force normal to the flow                               |
| $F_0$                   | Amplitude of the oscillatory force due to vortex shedding            |
| $\mathcal{F}$           | Fourier transform of velocity  |
| $k$                     | Spring constant  |
| $m$                     | Mass of the body   |
| $m_a$                   | Added mass   |
| $P_d$                   | Power dissipated due to mechanical damping                           |
| $P_{in} = \rho U^3 D/2$ | Energy flux of the approaching flow                                  |
| $P_m$                   | Mean power   |
| $P_t$                   | Power transferred to the body by the fluid                           |
| $t$                     | Time   |
| $U$                     | Freestream velocity  |
| $U_i$                   | Induced velocity   |
| $y, \dot{y}, \ddot{y}$  | Transverse displacement, velocity and acceleration of the body       |
| $\mathcal{A} = DL$      | Frontal area of the body   |
| $\lambda$               | Inverse time scale of a galloping dominated flow                     |

|  |   |
|--|---|
| $\lambda_{1,2}$                          | Eigenvalues of linearized equation of motion  |
| $\rho$                                   | Fluid density   |
| $\omega_n = 2\pi f$                      | Natural angular frequency of the system   |
| $\omega_s$                               | Vortex shedding angular frequency   |
| $c^* = cD/mU$                            | Non-dimensionalised damping factor  |
| $C_y = F_y/0.5\rho U^2 DL$               | Normal (lift) force coefficient   |
| $m^* = m/\rho D^2 L$                     | Mass ratio  |
| $Re$                                     | Reynolds number   |
| $U^* = U/fD$                             | Reduced velocity  |
| $Y = y/D$                                | Non-dimensional transverse displacement   |
| $\dot{Y} = m^* \dot{y}/a_1 U$            | Non-dimensional transverse velocity   |
| $\ddot{Y} = m^{*2} D \ddot{y}/a_1^2 U^2$ | Non-dimensional transverse acceleration   |
| $\Gamma_1 = 4\pi^2 m^{*2}/U^{*2} a_1^2$  | First dimensionless group arising from linearised,<br>Non-dimensionalised equation of motion  |
| $\Gamma_2 = c^* m^*/a_1$                 | Second dimensionless group arising from linearised,<br>Non-dimensionalised equation of motion |
| $\zeta = c/2m\omega_n$                   | Damping ratio   |
| $\theta = \tan^{-1}(\dot{y}/U)$          | Instantaneous angle of incidence (angle of attack)  |
| $\Pi_1 = 4\pi^2 m^{*2}/U^{*2}$           | Combined mass-stiffness parameter   |
| $\Pi_2 = c^* m^*$                        | Combined mass-damping parameter   |

## 2. Problem formulation and methodology

### 2.1. The quasi-steady state (QSS) model

The equation of motion of the body is given by

$$(m)\ddot{y} + c\dot{y} + ky = F_y, \quad (1)$$

where the forcing term  $F_y$  is given by

$$F_y = \frac{1}{2}\rho U^2 \mathcal{A} C_y. \quad (2)$$

In the QSS model, it is assumed that the force on the body at a given instantaneous incident angle  $\theta$  (defined in figure 1) is the same as the mean force on a static body at the same incident angle, or angle of attack. The instantaneous value of  $C_y$  is therefore determined by an interpolating polynomial based on the lift force data for flow over a stationary body at various  $\theta$ . For an oscillating body,  $\theta$  is related to the instantaneous transverse velocity

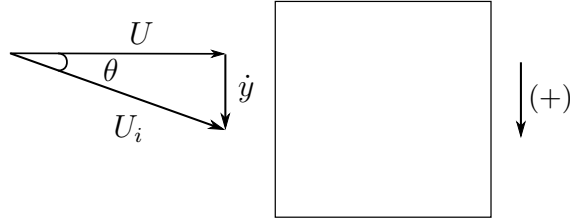


Figure 1: Induced angle of attack on the square prism due to the resultant of free-stream velocity of the fluid and transverse velocity of the body.

of the body  $\dot{y}$  as illustrated in figure 1. Therefore,  $C_y$  can be written as a function of  $\dot{y}$ .

The order of the interpolation polynomial for the lift force data has varied from study to study. For example a 7<sup>th</sup> order polynomial was used in Parkinson and Smith (1964) and 3<sup>rd</sup> order polynomial was used in Barrero-Gil et al. (2009). Ng et al. (2005) concluded that using a 7<sup>th</sup> order polynomial is sufficient and a polynomial higher than that of 7<sup>th</sup> order doesn't provide a significantly better result. Thus a 7<sup>th</sup> order interpolating polynomial is used in this present study. As a result,  $C_y(\theta)$  (noting that theta is proportional to  $\dot{y}/U$ ) is defined as

$$C_y(\theta) = a_1 \left( \frac{\dot{y}}{U} \right) + a_3 \left( \frac{\dot{y}}{U} \right)^3 + a_5 \left( \frac{\dot{y}}{U} \right)^5 + a_7 \left( \frac{\dot{y}}{U} \right)^7. \quad (3)$$

It is expected that vortex shedding will be well correlated along the span and provide significant forcing at low  $Re$ . Joly et al. (2012) introduced an additional sinusoidal forcing function to the fluid-dynamic forcing to model this. This enables the model to provide accurate predictions even at low mass ratios where galloping excitation is suppressed or not present. However, the strength of this additional forcing needs to be tuned in an *ad hoc* manner, and it is not clear how this forcing should vary with the other system parameters. Therefore, a focus of this study is to identify the parameter space where unmodified QSS model predicts power transfer accurately, and to quantify the error in the regions where it does not predict accurately. Therefore the additional sinusoidal forcing function is disregarded. Substituting the definition of the lift coefficient provided in equation (3) into the equation of motion of equation (2) gives

$$m\ddot{y} + c\dot{y} + ky = \frac{1}{2}\rho U^2 \mathcal{A} \left( a_1 \left( \frac{\dot{y}}{U} \right) + a_3 \left( \frac{\dot{y}}{U} \right)^3 + a_5 \left( \frac{\dot{y}}{U} \right)^5 + a_7 \left( \frac{\dot{y}}{U} \right)^7 \right). \quad (4)$$

This ordinary differential equation can be solved using standard time integration methods. In this study the fourth-order Runge-Kutta scheme built in to the MATLAB routine ‘ode45’ was used to obtain the solutions.

## 2.2. Calculation of average power

The dissipated power due to the mechanical damping represents the power transferred to the body from the fluid, and is the ideal potential amount of harvested power output before losses in any power take-off system are included. Therefore, the mean power output can be given by

$$P_m = \frac{1}{T} \int_0^T (c\dot{y})\dot{y}dt, \quad (5)$$

where  $T$  is the period of integration and  $c$  is the mechanical damping constant.

It should be noted that this quantity is equal to the work done on the body by the fluid, defined as

$$P_m = \frac{1}{T} \int_0^T F_y \dot{y}dt, \quad (6)$$

where  $F_y$  is the transverse (lift) force.

These two definitions show two important interpretations of the power transfer. The first shows that power is proportional to the mechanical damping and the magnitude of the transverse velocity. It is therefore tempting to think that the damping should be increased to increase the power transfer. In a power extraction device, the damping would be due to electric generator, and an increased damping would be due to an increased electrical resistance or load. However, very high damping will have the effect of reducing the velocity amplitude. Because of this, a balance needs to be found where the damping is high, but not so high that it overly suppresses the motion of the body.

The second shows that power will be high for situations where the transverse force and the body velocity are in phase. Therefore, simply increasing the magnitude of the force or velocity is not sufficient to increase the power transfer, if this increase in magnitude is linked to an increase in phase.

### 2.3. Parameters used

For the low  $Re$  tests, a value of  $Re = 200$  was used. Stationary  $C_y$  data were obtained at different angles of attack ranging from  $0^\circ$  to  $12^\circ$ . The average power was obtained by using equation 5, and the averaging was done over no less than 20 galloping periods. For the high  $Re$  tests, predictions of power output at  $Re = 22300$  were obtained using the coefficients for the  $C_y$  curve from Parkinson and Smith (1964) (Table (2)), in order to provide a comparison between high and low Reynolds numbers. The mass ratio  $m^*$  was kept at 1163 for  $Re = 22300$  (Similar to Parkinson and Smith (1964)) and  $m^* = 20$  for  $Re=200$ . These parameters were used throughout this study unless otherwise specified.

The stationary data for the low  $Re$  case and the DNS simulations of the fluid-structure interaction (FSI) problem were obtained using a high-order spectral element code to simulate the two-dimensional laminar flow. For all cases, a rectangular domain was employed where the inlet was placed  $20D$  from the centre of the body, while the outlet was situated  $60D$  away from the centre of the body. The lateral boundaries were placed  $20D$  away from the centre of the body. The Navier–Stokes equations were solved in an accelerated frame of reference attached to the moving body, along with the body equation of motion given in equation 1. A three-step time splitting scheme was used for the time integration. A time-dependent Dirichlet boundary condition was employed for the velocity on the inlet and lateral boundaries where  $u = U$  and  $v = -\dot{y}$  are the velocities in the  $x$  and  $y$  directions, respectively. A no-slip condition was enforced on the surface of the body. A Neumann condition, where the velocity gradient in the  $x$  direction was set to zero, was enforced on the outlet. A Neumann condition for the pressure, where the normal gradient was calculated from the Navier–Stokes equations, was employed on the inlet, lateral and body surface (Gresho and Sani, 1987), while a Dirichlet condition for the pressure ( $p = 0$ ) was enforced at the outlet. The details of the method can be found in Thompson et al. (2006, 1996), and a description of the spectral element method in general can be found in Karniadakis and Sherwin (2005). This code has been very well validated in a variety of fluid-structure interaction problems similar to that studied in this paper (Leontini et al., 2007; Griffith et al., 2011; Leontini et al., 2011; Leontini and Thompson, 2013).

The computational domain consists of 751 quadrilateral macro elements where the majority of the elements were concentrated near the square section. A freestream condition was given to the inlet, top and bottom boundaries



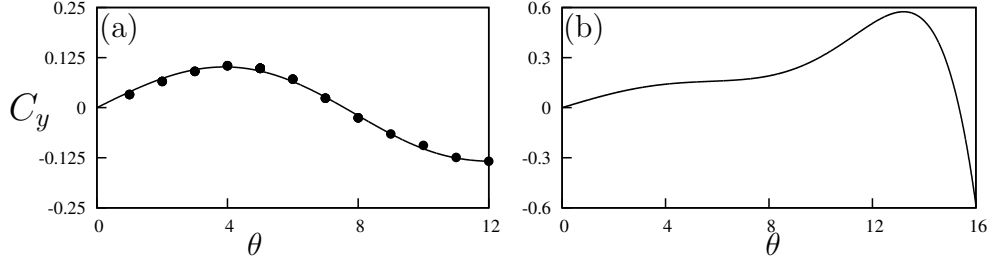


Figure 2: Lift coefficient,  $C_y$ , as a function of incidence angle  $\theta$ , for a static square cross section. (a) Data from simulations at  $Re = 200$  (b) data from Parkinson and Smith (1964) at  $Re = 22300$ . Points ( $\bullet$ ) are measurements from the simulations. At  $Re = 200$ . Curves in both plots are 7th-order interpolating polynomials used to predict the fluid forcing for the QSS model.  $C_y$  is the force coefficient of the force which occurs normal to the induced velocity.

and the normal velocity gradient was set to zero at the outlet. A convergence study was performed by changing the order of the polynomial ( $p$ -refinement) at  $U^* = 40$  and  $Re = 200$ . A 9<sup>th</sup> order polynomial together with a time step of  $\Delta t U/D = 0.001$  was sufficient to ensure an accuracy of 2% with regards to amplitude of oscillation.

### 3. Results

#### 3.1. Static body results

Figure 2 shows the plots  $C_y$  as a function of  $\theta$ , as well as the interpolation polynomials. For high  $Re$  the polynomial incorporated by Parkinson and Smith (1964) was used. For low  $Re$  a 7<sup>th</sup> order polynomial was fitted using nonlinear least-squares regression. The coefficients of these polynomial fits are shown in table 2.

There are several differences that can be observed between high and low Reynolds number data. The peak value of  $C_y$  is significantly lower at  $Re = 200$  ( $C_y = 0.12$  at  $5^\circ$ ) compared to  $Re = 22300$  ( $C_y = 0.57$  at  $13^\circ$ ). The inflection point present around  $8^\circ$  for  $Re = 22300$  is not present at  $Re = 200$ . This agrees with the findings of Luo et al. (2003). It was concluded by Luo et al. (2003) that hysteresis in the system response occurs due to the inflection point in the  $C_y$  curve. Therefore hysteresis is not expected at  $Re = 200$ .

The range of incident flow angles where  $C_y$  remains positive is narrow at  $Re = 200$  ( $0^\circ < \theta \leq 7^\circ$ ) compared to  $Re = 22300$  ( $0^\circ < \theta \leq 15^\circ$ ). This feature is what sustains galloping. Power is only transferred from the

| Case         | $a_1$ | $a_3$ | $a_5$  | $a_7$   |
|--------------|-------|-------|--------|---------|
| $Re = 200$   | 2.32  | 197.8 | 4301.7 | 30311.9 |
| $Re = 22300$ | 2.69  | 168   | 1670   | 59900   |

Table 2: Coefficient values used in the 7th order interpolation polynomial for high ( $Re = 22300$ ) and low ( $Re = 200$ ) Reynolds numbers. These data are used as input data to calculate the right-hand side of Eq. 4 throughout this study.

fluid to the supporting structure within this range of incident angles because fluid forces are acting in the direction of travel of, or in phase with, the oscillating body as demonstrated by equation 6. Incident angles beyond this range actually suppress the galloping and power is transferred in the opposite direction, i.e; from body to fluid. Therefore due to the overall smaller  $C_y$  and narrow range of angles where  $C_y$  is positive for  $Re = 200$  compared to  $Re = 22300$ , it is expected that the transferred power at  $Re = 200$  is significantly lower than at  $Re = 22300$ .

### 3.2. Formulation of the new dimensionless groups $\Pi_1$ and $\Pi_2$

The natural time scales of the system can be found by solving for the eigenvalues of the linearised equation of motion, namely

$$m\ddot{y} + c\dot{y} + ky = \frac{1}{2}\rho U^2 \mathcal{A}a_1 \left( \frac{\dot{y}}{U} \right), \quad (7)$$

which is a simplified version of the equation of motion presented in equation 4 with the polynomial series for the lift force truncated at the linear term.

Combining the  $\dot{y}$  terms and solving for eigenvalues gives

$$\lambda_{1,2} = -\frac{1}{2} \frac{c - \frac{1}{2}\rho U \mathcal{A}a_1}{m} \pm \frac{1}{2} \sqrt{\left[ \frac{c - \frac{1}{2}\rho U \mathcal{A}a_1}{(m)} \right]^2 - 4 \frac{k}{m}}. \quad (8)$$

If it is assumed that the spring is relatively weak,  $k \rightarrow 0$ , a single non-zero eigenvalue remains. This eigenvalue is

$$\lambda = -\frac{c - \frac{1}{2}\rho U \mathcal{A}a_1}{m}. \quad (9)$$

Further, if it is assumed that the mechanical damping is significantly weaker than the fluid-dynamic forces on the body,  $c \rightarrow 0$  and

$$\lambda = \frac{\frac{1}{2}\rho U A a_1}{m}. \quad (10)$$

In this form,  $\lambda$  represents the inverse time scale of the motion of the body due to the effect of the long-time fluid-dynamic forces. In fact, the terms can be regrouped and  $\lambda$  written as

$$\lambda = \frac{a_1}{m^*} \frac{U}{D} \quad (11)$$

Written this way, the important parameters that dictate this inverse time scale are clear. The rate of change in the fluid-dynamic force with respect to angle of attack when the body is at the equilibrium position,  $\partial C_y / \partial \alpha$ , is represented by  $a_1$ . The mass ratio is represented by  $m^*$ . The inverse advective time scale of the incoming flow is represented by the ratio  $U/D$ . Increasing  $a_1$  would mean the force on the body would increase more rapidly with small changes in the angle of attack,  $\theta$ , or transverse velocity. Equation 11 shows that such a change will increase the inverse time scale, or analogously decrease the response time of the body. Increasing the mass of the body, thereby increasing  $m^*$ , has the opposite effect. The inverse time scale is decreased, or as might be expected, a heavier body will respond more slowly.

This timescale can then be used to non-dimensionalize the equation of motion, and to find the relevant dimensionless groups of the problem. If the non-dimensional time,  $\tau$ , is defined such that  $\tau = t(a_1/m^*)(U/D)$ , the equation of motion presented in equation 4 can be non-dimensionalized as

$$\ddot{Y} + \frac{m^*}{a_1^2} \frac{kD^2}{mU^2} Y = \left( \frac{1}{2} - \frac{m^*}{a_1} \frac{cD}{mU} \right) \dot{Y} - \frac{a_1 A_3}{m^{*2}} \dot{Y}^3 + \frac{a_1^3 a_5}{m^{*4}} \dot{Y}^5 - \frac{a_1^5 a_7}{m^{*6}} \dot{Y}^7. \quad (12)$$

The coefficients can be regrouped into combinations of non-dimensional groups, and rewritten as

$$\ddot{Y} + \frac{4\pi^2 m^{*2}}{U^{*2} a_1^2} Y = \left( \frac{1}{2} - \frac{c^* m^*}{a_1} \right) \dot{Y} - \frac{a_1 A_3}{m^{*2}} \dot{Y}^3 + \frac{a_1^3 a_5}{m^{*4}} \dot{Y}^5 - \frac{a_1^5 a_7}{m^{*6}} \dot{Y}^7, \quad (13)$$

where  $U^*$  is the reduced velocity typically used as an independent variable in vortex-induced vibration studies and  $c^* = cD/mU$  is a non-dimensional damping parameter.

Equation 13 shows there are five non-dimensional parameters that play a role in setting the response of the system. These are the stiffness (represented by the reduced velocity  $U^*$ ), the damping  $c^*$ , the mass ratio  $m^*$ , and the geometry and  $Re$ , represented by the coefficients of the polynomial fit to the  $C_y$  curve,  $a_n$ . The grouping of these parameters into two groups in equation 13 which arise by non-dimensionalising using the natural time scale of the galloping system, suggests there are two groups that dictate the response:  $\Gamma_1 = 4\pi^2 m^{*2}/U^{*2} a_1^2$  and  $\Gamma_2 = c^* m^*/a_1$ . For a given geometry and Reynolds number,  $\Gamma_1$  can be thought of as a combined mass-stiffness, whereas  $\Gamma_2$  can be thought of as a combined mass-damping parameter. As it is assumed that during galloping the stiffness plays only a minor role,  $\Gamma_2$  seems a likely parameter to collapse the data. In fact, in the classic paper on galloping from Parkinson and Smith (1964), galloping data from wind tunnel tests is presented in terms of a parameter that can be shown to be the same as  $\Gamma_2$ .

All of the quantities that make up  $\Gamma_1$  and  $\Gamma_2$  can, in theory, be known before an experiment is conducted. However, the quantity  $a_1$  is a relatively difficult one to determine, requiring static body experiments or simulations. Here, the geometry is unchanged and results are only being compared at the same  $Re$ . Hence, suitable parameters can be formed by multiplying  $\Gamma_1$  and  $\Gamma_2$  by  $a_1^2$  and  $a_1$  respectively, to arrive at a mass-stiffness parameter  $\Pi_1 = 4\pi^2 m^{*2}/U^{*2}$ , and a mass-damping parameter defined as  $\Pi_2 = c^* m^*$ .

### 3.3. Comparison of $\Pi_1$ and $\Pi_2$ with classical VIV parameters

Another fluid-structure interaction phenomenon, vortex-induced vibration (VIV), has also been investigated as a candidate for the power extraction from flows. The work from Bernitsas et al. (2008, 2009); Raghavan and Bernitsas (2011); Lee and Bernitsas (2011) and others from the same group at the University of Michigan have made significant progress with this problem. Therefore it may seem, at least initially, reasonable to present data from the fluid-elastic problem in the same parameters as typically used in VIV studies.

Figure 3 shows the comparison of mean power data at  $Re = 200$  presented using different independent variables. Subfigures (a), (c) and (e) show the displacement amplitude, velocity amplitude and the mean power as a function of the classic VIV parameter,  $U^*$  for various damping ratios  $\zeta$ . Subfigures (b), (d) and (f) shows the same data as a function of  $\Pi_2$ , for various, reasonably high values of  $\Pi_1$ , as defined above in section 3.2. The data presented using the classical VIV parameters follows the same trends as Barrero-Gil et al.

(2010). However, the data presented using the dimensionless group formulated using the natural time scales of the system shows an excellent collapse for both velocity amplitude and mean power, showing that the power is essentially dictated by  $\Pi_2$ . This implies that unlike VIV which is a type of resonant phenomenon, the natural frequency of the system which is used to scale  $U^*$ ,  $\zeta$  and  $\Pi_1$  does not have a large influence on the system behaviour in these cases.

#### 3.4. Comparison of power between high and low $Re$ data

The marked success of the collapse using  $\Pi_2$  for the  $Re = 200$  case, particularly of the mean power, could also be replicated for the higher  $Re$  case at  $Re = 22300$ . Figure 4 presents the mean power for both the high and low  $Re$  cases for selected values of  $\Pi_1$ . It is shown that the data collapse in both cases, demonstrating the validity of using  $\Pi_2$  as an independent variable.

Hysteresis could be observed for the  $Re = 22300$  case. The different solutions could be obtained by manipulating the initial conditions (initial displacement) of the system. The upper branch was obtained by giving an initial displacement which was higher than the expected amplitude while the lower branch was obtained by providing a lower initial displacement than the expected amplitude. Although theory shows a possible third state, it is an unstable branch and as such it could not be achieved numerically. This was also observed by Vio et al. (2007).

#### 3.5. Dependence on mass-stiffness, $\Pi_1$

The results of sections 3.3 and 3.4 show that the mean extracted power is essentially a function of a single variable, the combined mass-damping  $\Pi_2$ . However, the timescale analysis of section 3.2 showed that a second variable, the combined mass-stiffness  $\Pi_1$  should also play a role. Here, the impact of this variable is investigated further. Overall, the system behaviour can be separated into two wide regimes; that for “high”  $\Pi_1$  and that for “low”  $\Pi_1$ . These two regimes are further investigated and explained in this following section.

Figure 5 shows the mean power as a function of  $\Pi_2$  for a range of values of  $\Pi_1$ . Two subfigures are shown; subfigure (a) shows data for  $\Pi_1 \geq 10$ , while (b) shows data for  $\Pi_1 \leq 10$ . In figure 5(a), the collapse of the mean power is excellent, showing that for  $\Pi_1 \geq 10$ , the mean power is independent of  $\Pi_1$ .

For low values of  $\Pi_1 \leq 10$ , figure 5(b) shows that the predicted mean power increases as  $\Pi_1$  is decreased, indicating that the mean power is a weak

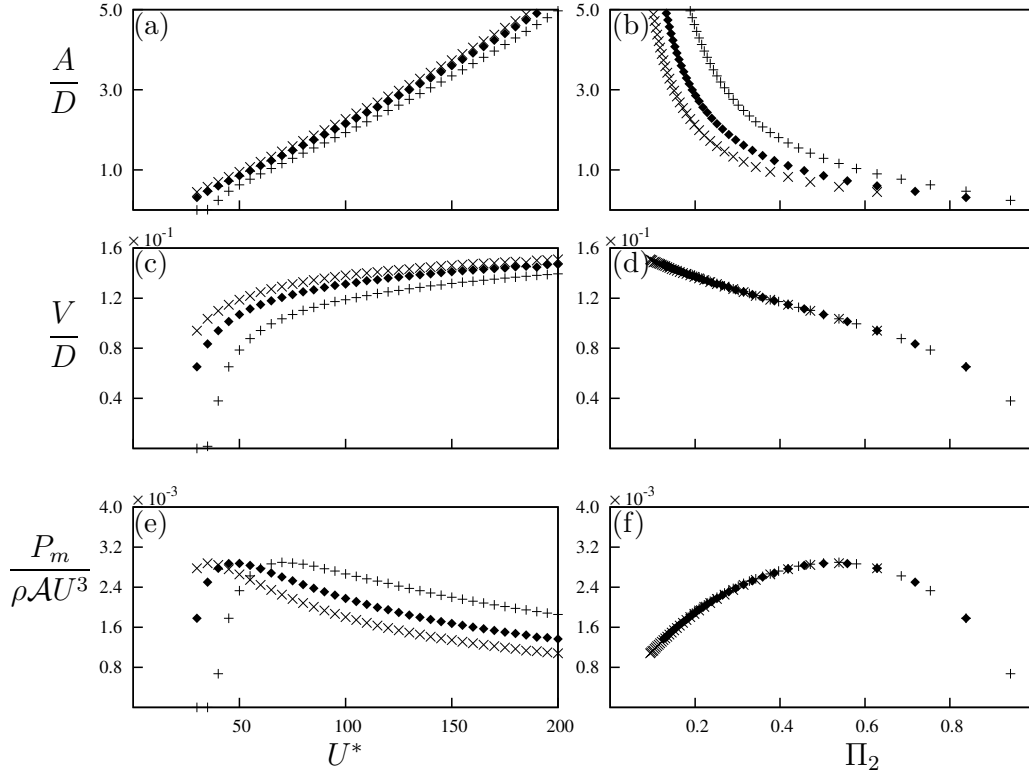


Figure 3: Displacement amplitude, velocity amplitude and mean power data as functions of two different independent variables. Data presented in (a), (c) and (e) using the classical VIV parameter  $U^*$ , obtained at  $Re = 200$  and  $m^* = 20$  at three different damping ratios:  $\zeta = 0.075$  ( $\times$ ),  $\zeta = 0.1$  ( $\blacklozenge$ ) and  $\zeta = 0.15$  ( $+$ ). (b) (d) and (f) are the same data presented using the combined mass-damping parameter ( $\Pi_2$ ) as the independent variable. Even though  $\Pi_1$  varies in the range of  $0.4 \leq \Pi_1 \leq 17.5$ , it is clear that the power is a function of  $\Pi_2$  only.

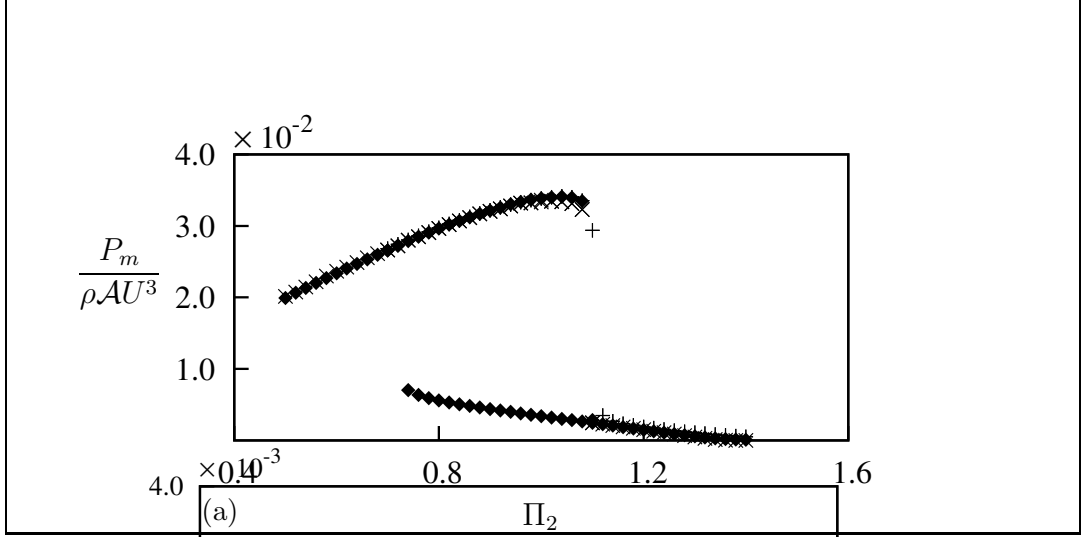


Figure 4: Mean power as a function of  $\Pi_2$ . Data presented at (a)  $Re = 22300$ ,  $\Pi_1 = 2000$  ( $\times$ ),  $\Pi_1 = 10000$  ( $+$ ). Hysteresis could be observed at high  $Re$ .

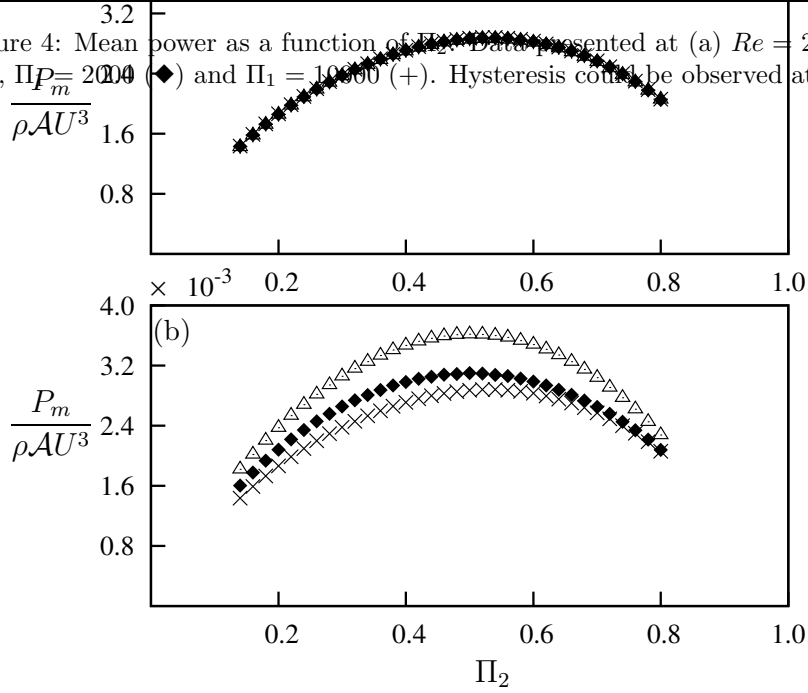


Figure 5: Mean power as a function of  $\Pi_2$  obtained using the QSS model at  $Re = 200$ . (a) High  $\Pi_1$ ; data presented at four different combined mass-stiffness levels.  $\Pi_1 = 10$  ( $m^* = 20$ ,  $U^* = 40$ ) ( $\times$ ),  $\Pi_1 = 100$  ( $m^* = 80$ ,  $U^* = 50$ ) ( $+$ ),  $\Pi_1 = 500$  ( $m^* = 220$ ,  $U^* = 60$ ) ( $\blacklozenge$ ) and  $\Pi_1 = 1000$  ( $m^* = 400$ ,  $U^* = 40$ ) ( $\triangle$ ). (b) Low  $\Pi_1$ ; data presented at  $\Pi_1 = 10$  ( $\times$ ),  $\Pi_1 = 0.1$  ( $\blacklozenge$ ), and  $\Pi_1 = 0.01$  ( $\triangle$ ).

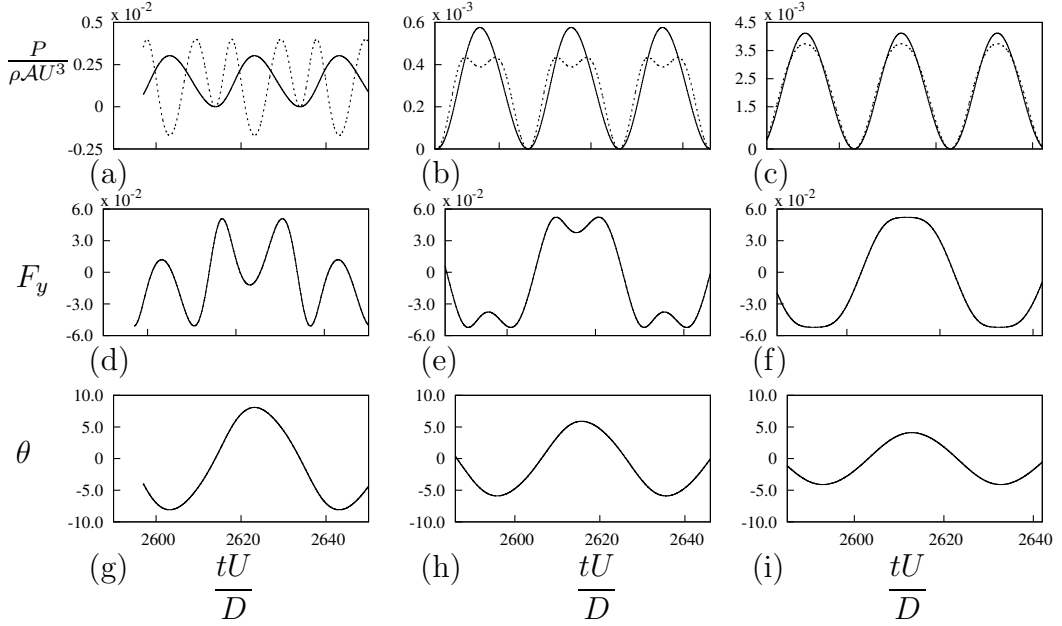


Figure 6: Time histories of  $P_t$ ,  $P_d$ ,  $F_y$  and  $\theta$  at  $\Pi_2 = 0.15, 0.54$  and  $0.8$  from the QSS model. Data was obtained at  $m^* = 20$ ,  $\Pi_1 = 10$  and  $Re=200$ . The time histories of  $P_t$  (—) and  $P_d$  (---) are presented for: (a)  $\Pi_2 = 0.15$ ; (b)  $\Pi_2 = 0.54$ ; (c)  $\Pi_2 = 0.8$ . Time histories of the instantaneous force  $F_y$  for: (d)  $\Pi_2 = 0.15$ ; (e)  $\Pi_2 = 0.54$ ; (f)  $\Pi_2 = 0.8$ . Time histories of the instantaneous angle  $\theta$  for: (g)  $\Pi_2 = 0.15$ ; (h)  $\Pi_2 = 0.55$ ; (i)  $\Pi_2 = 0.8$ .

function of  $\Pi_1$  at low  $\Pi_1$  levels. This provides the distinction between high and low  $\Pi_1$  regimes. For high values where  $\Pi_1 \geq 10$ , the mean extracted power is a function of  $\Pi_2$  only; for low values where  $\Pi_1 < 10$ , the mean extracted power is a weak function of  $\Pi_1$ .

Regardless of the value of  $\Pi_1$ , the variation of the mean extracted power with  $\Pi_2$  is essentially the same. With increasing  $\Pi_2$ , the mean extracted power initially increases, before reaching some maximum value and then decreasing. This relationship between power and  $\Pi_2$  can be explained by analysing the time histories of selected cases. Data at  $\Pi_1 = 10$ ,  $m^* = 20$  and  $Re = 200$  are shown in figure 6 and are analysed as an example. Values of  $\Pi_2$  less than (region 1), equal to (region 2), and greater than (region 3) the value where the mean extracted power is a maximum are analysed as examples.

The instantaneous power from the fluid to the body can be expressed as  $P_t = F_y \dot{y}$ . Similarly the dissipated power due to the mechanical damping can be expressed as  $P_d = (c\dot{y})\dot{y}$ . The time average of these two quantities,



described in equations 5 and 6 must be equal due to energy conservation.

At region 1 ( $\Pi_2 = 0.3$ ) the damping is low in comparison with region 2 and 3. While this may lead to larger oscillations, damping is required to dissipate and therefore extract power according to equation 5. Therefore, the low damping in this region leads to a low mean power output. Fig.6 (a) shows that  $P_d$  (the power dissipated by damping) becomes negative over some portion of the cycle. This is caused by the high velocity amplitude leading to the equivalent incident angle  $\theta$  to exceed the range where  $C_y$  is positive (i.e.  $0 < \theta < 6^\circ$  as shown in figure3(a)). In this portion of the cycle the fluid-dynamic force actually opposes the direction of travel and power is transferred from the structure to the fluid during those times. From an energy perspective, the mechanical damping is not sufficient to remove the energy transferred from the fluid to the structure through work during other times of the cycle because  $\Pi_2$  is substantially low. Therefore this excess energy is transferred back to the fluid as depicted by the negative region of  $P_d$ .

At region 3 where  $\Pi_2 = 0.8$  the damping constant is high and a clear sinusoidal signal is observed for both  $P_d$  and  $P_t$  in figure 6(c). Figures 6(f) and 6(i) show that equivalent incident angle  $\theta$  (which for small values, is proportional to the transverse velocity of the body) is in phase with  $F_y$ . The velocity amplitude in this case is small and  $\theta$  is within the range where the fluid-dynamic force increases with the incident angle (i.e.  $0 < \theta \leq 5^\circ$  as shown in figure 2(a)). According to equation 6, these conditions are suitable for high power output. However in this case, the high damping limits the velocity amplitude and results in relatively low fluid dynamic forces.

At region 2 ( $\Pi_2 = 0.54$ ), a balance is found between high and low values of damping.  $P_d$  is not a pure sinusoidal signal, however the signal remains periodic. From the time history graph of  $P_d$ , two ‘peaks’ are present in a single half cycle as shown in figure 6(b). In this case, the velocity amplitude actually exceeds the equivalent incident angle where the fluid-dynamic forces peaks (i.e.  $\theta = 5^\circ$  in 3 (a)). The dips in  $P_d$  between the two peaks approximately correspond to the time where the transverse velocity is higher than 0.09 and  $F_y$  is decreasing with increasing transverse velocity. The mean power output is at its maximum. This is due to the fact that this region is the best compromise between region 1 and 3. The damping is high enough to obtain a high power output while not so high that the motion is completely suppressed.

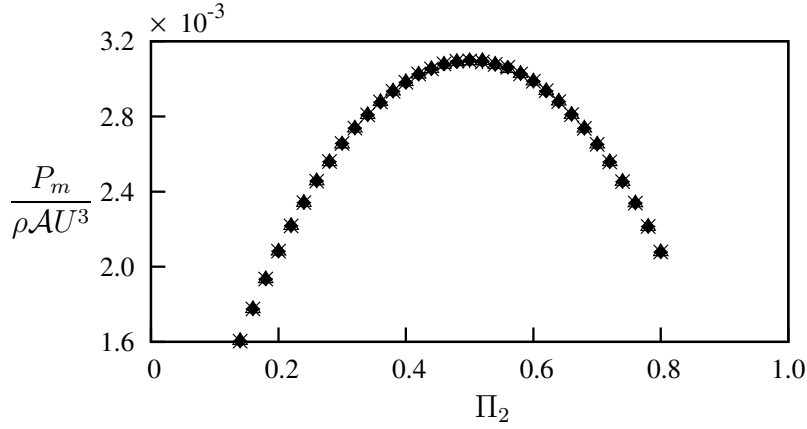


Figure 7: Mean power as a function of  $\Pi_2$  obtained using QSS model at  $\Pi_1 = 0.1$ . Data presented at  $m^* = 2$  ( $\blacklozenge$ ),  $m^* = 20$  ( $\triangle$ ) and  $m^* = 50$  (\*). The mass ratio does not have an effect on  $\Pi_1$  even at low  $\Pi_1$ .

### 3.6. Dependence on the mass ratio $m^*$

While for high values of  $\Pi_1$  it is clear that the mean extracted power is a function of  $\Pi_2$  only, a question arises for low values of  $\Pi_1$ ; is the variation in the mean extracted power purely a function of  $\Pi_1$ , or is it also a function of the mass ratio  $m^*$ ? To answer this question, the model has been solved for a fixed value of  $\Pi_1$ , but for varying values of  $m^*$ . This means that  $\Pi_1$  was varied by changing the system stiffness.

Figure 7 shows the mean extracted power as a function of  $\Pi_2$ , for a fixed  $\Pi_1 = 0.1$ , for three different values of  $m^*$ . From the figure it is clear that the results are independent of  $m^*$ , and are a function of  $\Pi_1$  and  $\Pi_2$  only.

### 3.7. Comparison with DNS data

The QSS model assumes that the only force driving the system is the instantaneous lift generated by the induced velocity. However, vortex shedding is also present in this system. Therefore, an essential assumption when this model is used, is that the effect of vortex shedding is minimal. Hence, the model has been always used at high  $Re$  and at high mass ratios. The present study is focused on identifying the limiting parameters of the QSS model at low Reynolds numbers by providing a comparison with DNS results.

Joly et al. (2012) showed that the displacement data obtained using the QSS assumption and DNS agree well at low Reynolds numbers, with the modification implemented to the oscillator equation which accounts for the

vortex shedding. These data were obtained at zero damping levels. However, the current study is focused on the behaviour and the power transfer of the system. Therefore analysing the behaviour of the system with increasing damping is of interest.

The comparison between QSS and the DNS results is presented in figure 13. The maximum displacement, velocity and mean extracted power are presented as a function of  $\Pi_2$ . A range of values of  $\Pi_1$  are compared to the QSS model data for  $\Pi_1 = 10$ . Figures 13(a) and 13(b) show little variation with  $\Pi_1$ , and the comparison between the QSS model and the DNS simulations is quite good. However, the mean extracted power shown in figure 13(c) reveals that the mean power is influenced by both  $\Pi_1$  and  $\Pi_2$ . This is particularly clear for low values of  $\Pi_1$ , where the discrepancy between the QSS model predictions of power and the DNS simulations is the largest. Comparing figure 13(c) with figure 5(b) shows that  $\Pi_1$  has much more influence on the power extracted than predicted by the QSS model. In fact, the QSS model predicts that the mean extracted power should increase with decreasing  $\Pi_1$ , whereas the DNS simulations show that the mean extracted power decreases with decreasing  $\Pi_1$ .

Figure 9(a) clearly shows the dependence of the mean extracted power on  $\Pi_1$ . Here, the maximum power extracted for a given value of  $\Pi_1$ , over all values of  $\Pi_2$  (essentially the value of extracted power at the turning point), is plotted as a function of  $\Pi_1$ . These values were obtained by fitting a quadratic to the data of figure 7 and finding the value of mean extracted power at the turning point. The rapid decrease in the extracted power as  $\Pi_1 \rightarrow 0$  is clear.

Figure 9(a) also shows that  $\Pi_1$  is important to higher values than predicted by the QSS model. For the QSS model, the mean extracted power was essentially independent of  $\Pi_1$  for  $\Pi_1 > 10$ , as shown by the open symbols on the figure. However, the mean extracted power from the DNS data shows a significant dependence on  $\Pi_1$  for  $\Pi_1 < 250$ . Even so, the power extracted during the DNS simulations converges to the value predicted by the QSS model as  $\Pi_1$  increases.

Figure 9(b) shows the value of  $\Pi_2$  at which the turning point, and therefore the maximum power output, occurs. The open symbols show the value predicted by the QSS model, the closed symbols show the value predicted by the DNS. The two are not the same, with a value around 0.41 predicted by the DNS (shown with a dashed line) and a value above 0.5 predicted by the QSS model. However, both models show that while the power extracted is a reasonably strong function of  $\Pi_1$ , the value of  $\Pi_2$  at which this maximum

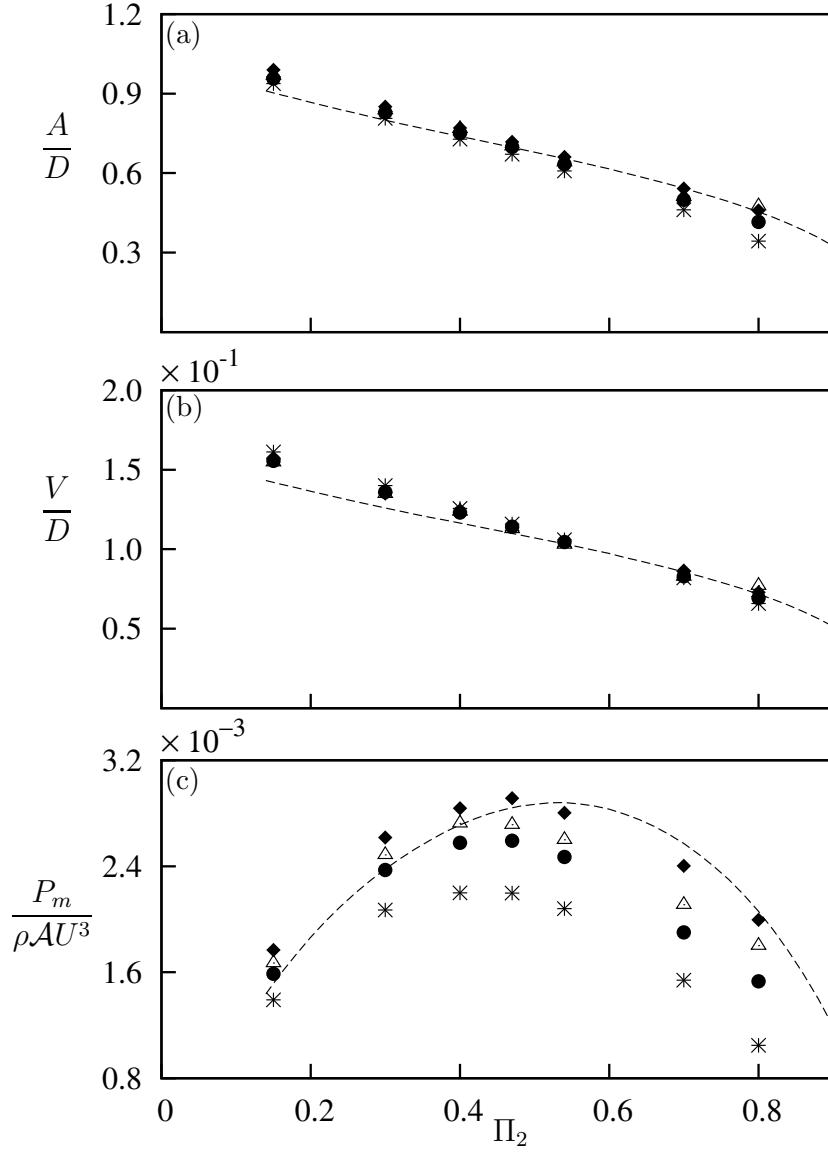


Figure 8: Comparison of data generated using the quasi-static model and full DNS simulations at. (a) Displacement amplitude, (b) velocity amplitude and (c) mean power as functions of  $\Pi_2$ . Data were obtained at  $Re = 200$  at four values  $\Pi_1 = 10$  ( $m^* = 20.13$ ) (\*),  $\Pi_1 = 60$  ( $m^* = 49.31$ ) (●),  $\Pi_1 = 250$  ( $m^* = 100.7$ ) (△) and  $\Pi_1 = 1000$  ( $m^* = 201.3$ ) (◆). The QSS data at  $\Pi_1 = 10$  (---).

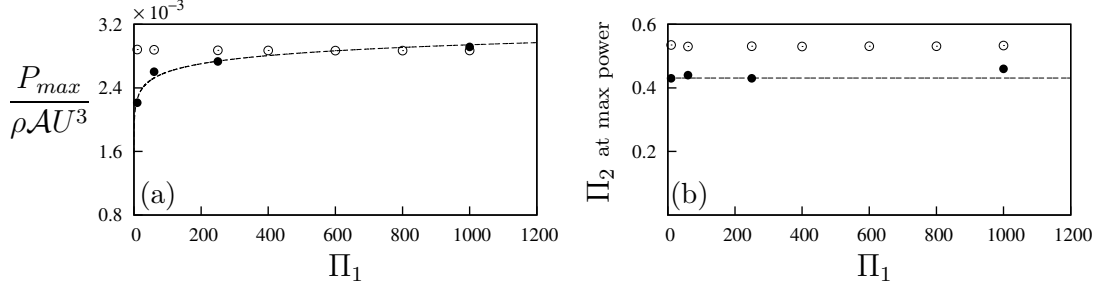


Figure 9: (a) Maximum power and (b) the value of  $\Pi_2$  at maximum power of QSS data (○) and DNS data (●), as functions of  $\Pi_1$ . For the DNS data, The maximum power asymptotes to an upper value with increasing  $\Pi_1$ , while the value of  $\Pi_2$  where maximum power occurs is relatively insensitive to  $\Pi_1$ . The maximum power of the QSS data remains relatively constant, as does the value of  $\Pi_2$  where maximum power occurs. The dash curve (---) of (a) follows the logarithmic fit of the maximum power which is  $P_{max}/\rho AU^3 = 1.48 \times 10^{-4} \ln(\Pi_1) + 1.9 \times 10^{-3}$ . The dashed curve in (b) shows the value  $\Pi_2 \simeq 0.43$ .

power occurs is relatively unaffected.

In an effort to further quantify the performance of the QSS model, the percentage between the QSS and DNS extracted power data as a function of  $\Pi_1$  was calculated using the equation

$$\% \text{ error} = \left| \frac{P_{m(QSS)} - P_{m(DNS)}}{P_{m(DNS)}} \right| \times 100. \quad (14)$$

The results of this calculation are plotted in figure 10, along with a power-law best fit  $138.697\Pi_1^{-0.6}$ . The figure clearly shows that as  $\Pi_1$  increases, the error between the QSS and DNS models quickly decreases. However, at low values of  $\Pi_1$ , the discrepancy between the two can be quite large, around 30%.

A likely reason for this discrepancy at low  $\Pi_1$  is the influence of the vortex shedding, which is not accounted for in the QSS model. To investigate this further, frequency spectra for the body velocity from DNS cases at varying values of  $\Pi_1$ , at a value of  $\Pi_2 = 0.47$  (close to the value at which the mean extracted power is a maximum), have been produced. They are presented, along with the original time histories in figure 11.

This figure shows the velocity signals at  $\Pi_1 = 0.8$  and  $\Pi_2 = 10, 60, 250$  and 1000 and the corresponding spectrum. The spectral data shows a significant component around  $fd/U = 0.156$  which can be identified as the vortex

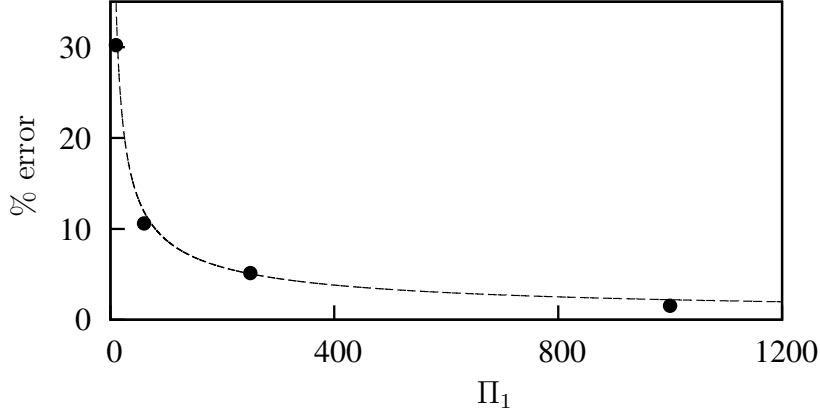


Figure 10: The percentage error between the maximum power obtained using DNS data and predicted by QSS model as a function of  $\Pi_1$ . The QSS model prediction is worst for low values of  $\Pi_1$ . The dash curve (---) follows the power law fit of the percentage error which is  $\%error = 138.697\Pi_1^{-0.6}$ .

shedding frequency. The magnitude of the component at the vortex shedding frequency clearly reduces as  $\Pi_1$  is increased. This indicates that the influence of vortex shedding is much more prominent at low  $\Pi_1$ , therefore resulting in larger deviations from quasi-steady state results. This builds on the work of Joly et al. (2012), which was conducted at zero damping, that implied that mean extracted power would be influenced by vortex shedding at low mass.

This influence is explicitly shown here. Figure 12 plots the relative intensity of the component at the vortex shedding frequency to the component at the galloping or oscillation frequency in the spectra of figure 11.

Similar to the discrepancy between the QSS and DNS mean extracted power shown in figure 10, the relative strength of the vortex shedding is seen to be large at small values of  $\Pi_1$ , and quickly decreases as  $\Pi_1$  is increased. The figure shows that the relative power of the vortex shedding frequency to the galloping frequency is  $0.977\Pi_1^{-0.52}$ .

The difference between the power predicted by the QSS and DNS models scales with  $\Pi_1^{-0.6}$ ; the relative power at the vortex shedding frequency scales with  $\Pi_1^{-0.52}$ . These scalings are quite similar, and both are close to  $1/\sqrt{\Pi_1}$ . While not unequivocal, this correlation strongly indicates this discrepancy is due to the influence of the vortex shedding, even though the vortex shedding and galloping frequencies remain separated by around the same amount for all values of  $\Pi_1$  presented in figure 11. The data presented in figure 12 also

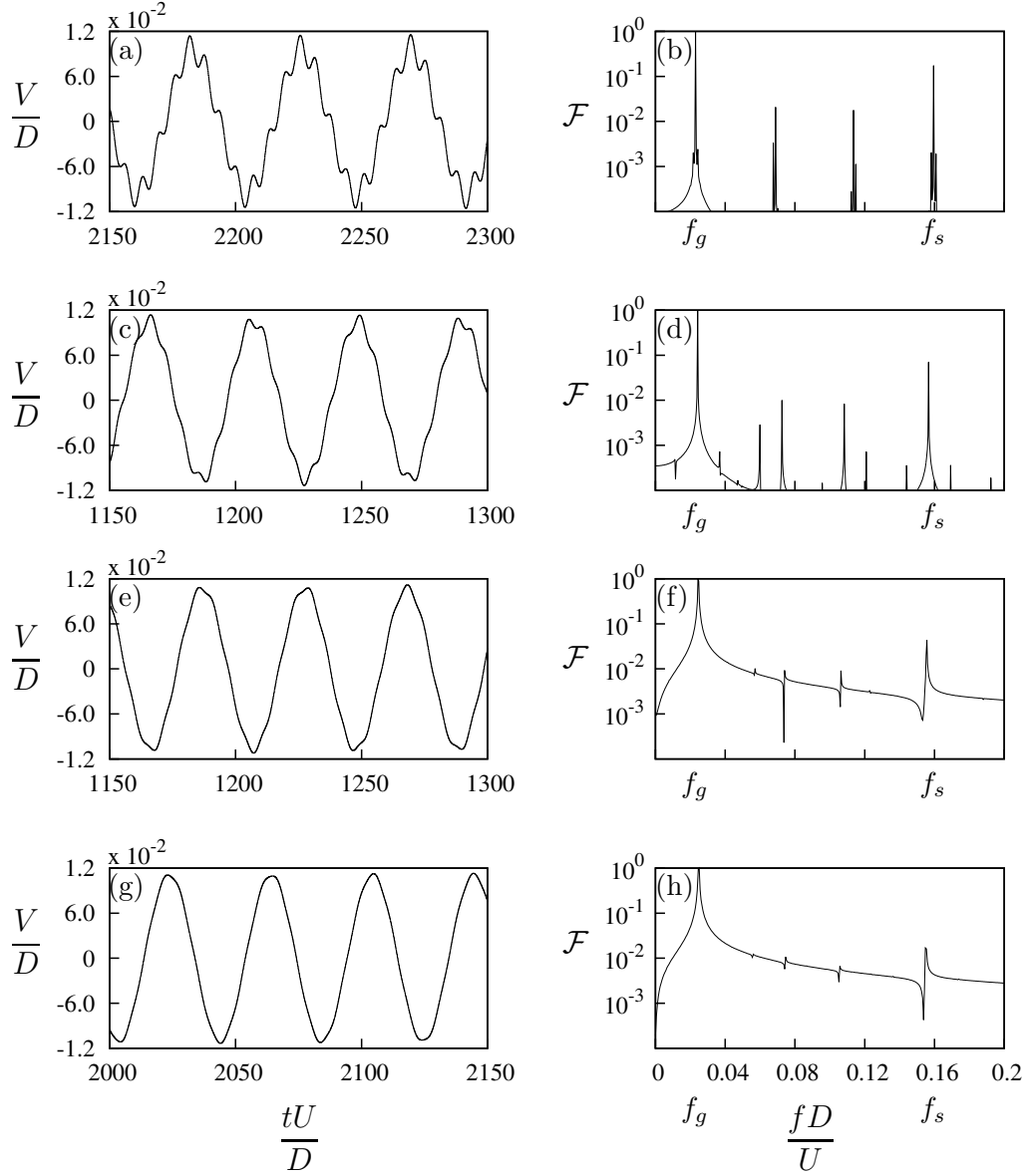


Figure 11: Velocity signal (right) and the corresponding power spectrum (left) of the DNS data at four values of  $\Pi_1$  at  $\Pi_2 = 0.47$ . (a) and (b)  $\Pi_1 = 10$ , (c) and (d)  $\Pi_1 = 60$ , (e) and (f)  $\Pi_1 = 250$ , (g) and (h)  $\Pi_1 = 1000$ .  $U^*$  is kept at 40 therefore the mass ratio increases as  $\Pi_1$  increases. It is evident that the influence of vortex shedding reduces as the inertia of the system increases.

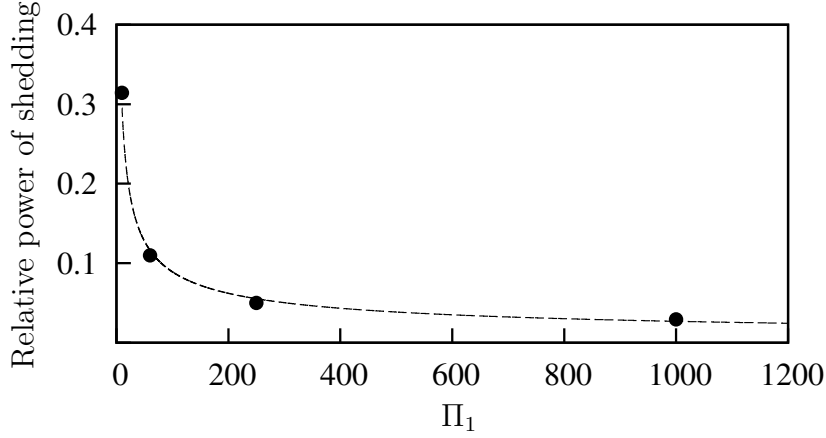


Figure 12: The relative power of the vortex shedding as a function of  $\Pi_1$ . The relative power of the vortex shedding decreases as  $\Pi_1$  increases. The dashed curve (---) follows the power law fit of the percentage error which is  $\text{Relative power} = 0.977\Pi_1^{-0.52}$ .

give some indication of the strength of any vortex shedding correction term that might be added to the QSS model in an effort to decrease the discrepancy between it and the DNS simulations.

#### 4. Conclusion

In this paper the power transfer of a square body under fluid-elastic galloping is analysed by solving the quasi-steady state oscillator model equation using numerical integration. The QSS model provides equations where dimensionless groups could be formulated using the relevant time scales. A good collapse for predicted output of power could be obtained using these dimensionless groups in comparison with the classical VIV parameters i.e.  $\zeta$  and  $U^*$ . The collapsed data using the dimensionless groups strengthens the argument that the velocity amplitude and the power transfer of the system does not depend on the natural frequency of the system.

In comparison with the direct numerical simulation data, it could be concluded that the QSS model provides a good estimate of the power output of the system when  $\Pi_1$  is relatively high. However at low values of  $\Pi_1$ , the prediction is not close due to the fact that the QSS model does not account for the impact of vortex shedding which is shown to increase in influence as  $\Pi_1$  is decreased. However, the QSS model does provide a reasonable prediction of the value of  $\Pi_2$  at which maximum power is produced. Both the error in



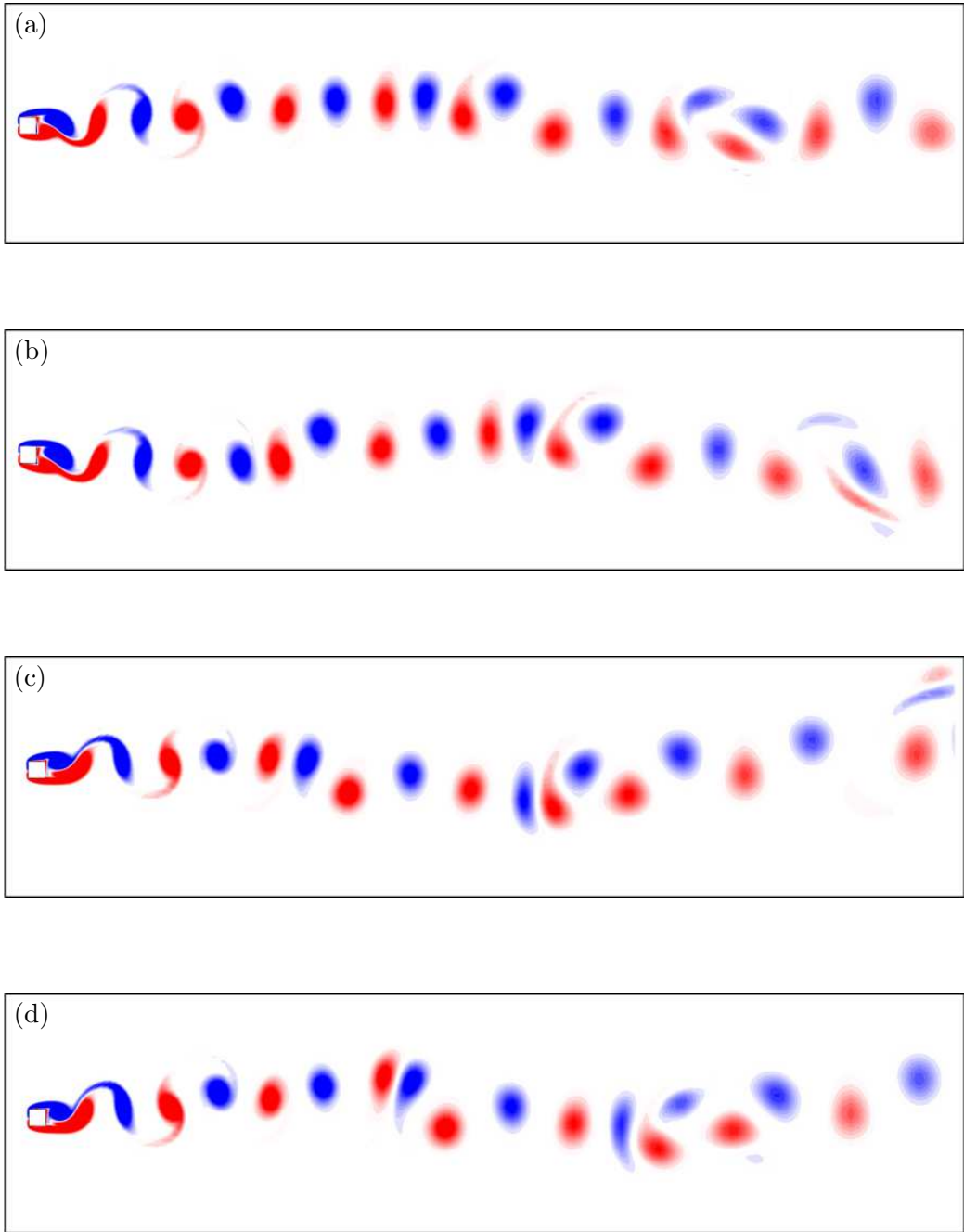


Figure 13: Vorticity plots of the flow at arbitrary positions at  $\Pi_2 = 0.47$ . (a)  $\Pi_1 = 10$ , (b)  $\Pi_1 = 60$  (c)  $\Pi_1 = 250$  and (d)  $\Pi_1 = 1000$  at  $Re = 200$ .

predicted maximum power between the QSS and the DNS models, and the relative power of the vortex shedding, scale similarly to  $1/\sqrt{\Pi_2}$ .

## References

- Barrero-Gil, A., Alonso, G., Sanz-Andres, A., Jul. 2010. Energy harvesting from transverse galloping. *Journal of Sound and Vibration* 329 (14), 2873–2883.
- Barrero-Gil, A., Sanz-Andrés, A., Roura, M., Oct. 2009. Transverse galloping at low Reynolds numbers. *Journal of Fluids and Structures* 25 (7), 1236–1242.
- Bernitsas, M. M., Ben-Simon, Y., Raghavan, K., Garcia, E. M. H., 2009. The VIVACE Converter: Model Tests at High Damping and Reynolds Number Around 10[sup 5]. *Journal of Offshore Mechanics and Arctic Engineering* 131 (1), 011102.
- Bernitsas, M. M., Raghavan, K., Ben-Simon, Y., Garcia, E. M. H., 2008. VIVACE (Vortex Induced Vibration Aquatic Clean Energy): A new concept in generation of clean and renewable energy from fluid flow. *Journal of Offshore Mechanics and Arctic Engineering* 130 (4), 041101–15.
- Den Hartog, J. P., 1956. *Mechanical Vibrations*. Dover Books on Engineering. Dover Publications.
- Glauert, H., 1919. The rotation of an aerofoil about a fixed axis. Tech. rep., Advisory Committee on Aeronautics R and M 595. HMSO, London.
- Gresho, P. M., Sani, R. L., 1987. On pressure boundary conditions for the incompressible Navier–Stokes equations. *International journal for numerical methods in fluids* 7, 1111–1145.
- Griffith, M. D., Leontini, J. S., Thompson, M. C., Hourigan, K., 2011. Vortex shedding and three-dimensional behaviour of flow past a cylinder confined in a channel. *Journal of Fluids and Structures* 27 (5-6), 855–860.
- Joly, A., Etienne, S., Pelletier, D., Jan. 2012. Galloping of square cylinders in cross-flow at low Reynolds numbers. *Journal of Fluids and Structures* 28, 232–243.
- Karniadakis, G. E., Sherwin, S., 2005. *Spectral/hp element methods for computational fluid dynamics*, ii Edition. Oxford University.

- Lee, J., Bernitsas, M., Nov. 2011. High-damping, high-Reynolds VIV tests for energy harnessing using the VIVACE converter. *Ocean Engineering* 38 (16), 1697–1712.
- Leontini, J. S., Lo Jacono, D., Thompson, M. C., Nov. 2011. A numerical study of an inline oscillating cylinder in a free stream. *Journal of Fluid Mechanics* 688, 551–568.
- Leontini, J. S., Thompson, M. C., 2013. Vortex-induced vibrations of a diamond cross-section: Sensitivity to corner sharpness. *Journal of Fluids and Structures* 39, 371–390.
- Leontini, J. S., Thompson, M. C., Hourigan, K., Apr. 2007. Three-dimensional transition in the wake of a transversely oscillating cylinder. *Journal of Fluid Mechanics* 577, 79.
- Luo, S., Chew, Y., Ng, Y., Aug. 2003. Hysteresis phenomenon in the galloping oscillation of a square cylinder. *Journal of Fluids and Structures* 18 (1), 103–118.
- Ng, Y., Luo, S., Chew, Y., Jan. 2005. On using high-order polynomial curve fits in the quasi-steady theory for square-cylinder galloping. *Journal of Fluids and Structures* 20 (1), 141–146.
- Païdoussis, M., Price, S., de Langre, E., 2010. *Fluid-Structure Interactions : Cross-Flow-Induced Instabilities*. Cambridge University Press.
- Parkinson, G. V., Smith, J. D., 1964. The square prism as an aeroelastic non-linear oscillator. *The Quarterly Journal of Mechanics and Applied Mathematics* 17 (2), 225–239.
- Raghavan, K., Bernitsas, M., Apr. 2011. Experimental investigation of Reynolds number effect on vortex induced vibration of rigid circular cylinder on elastic supports. *Ocean Engineering* 38 (5-6), 719–731.
- Thompson, M., Hourigan, K., Sheridan, J., Feb. 1996. Three-dimensional instabilities in the wake of a circular cylinder. *Experimental Thermal and Fluid Science* 12 (2), 190–196.
- Thompson, M. C., Hourigan, K., Cheung, A., Leweke, T., Nov. 2006. Hydrodynamics of a particle impact on a wall. *Applied Mathematical Modelling* 30 (11), 1356–1369.

Vio, G., Dimitriadis, G., Cooper, J., Oct. 2007. Bifurcation analysis and limit cycle oscillation amplitude prediction methods applied to the aeroelastic galloping problem. *Journal of Fluids and Structures* 23 (7), 983–1011.